Chemical Engineering Journal 437 (2022) 135302

Contents lists available at ScienceDirect

Chemical Engineering Journal

journal homepage: www.elsevier.com/locate/cej

Cu vacancy engineering of cage-compound $BaCu_2Se_2$: Realization of temperature-dependent hole concentration for high average thermoelectric figure-of-merit

Tianyao Weng [a,1], Zhili Li [a,1], Yang Li [a], Yao Hu [a], Kai Guo [a,b,*], Tao Liu [c], Jianxin Zhang [c], Wanyu Lyu [d], Lili Xi [c], Xinxin Yang [a], Ying Jiang [c,*], Jiong Yang [c], Jiye Zhang [a], Jun Luo [a,c]

[a] School of Materials Science and Engineering, Shanghai University, 99 Shangda Road, Shanghai 200444, PR China
[b] School of Physics and Materials Science, Guangzhou University, Guangzhou 510006, PR China
[c] Materials Genome Institute, Shanghai University, 99 Shangda Road, Shanghai 200444, PR China
[d] Centre for Future Materials, University of Southern Queensland, Springfield Central, QLD 4300, Australia

ARTICLE INFO

Keywords:
$BaCu_2Se_2$
Copper vacancy
Hole concentration
Defect energy level
Point defect scattering

ABSTRACT

Vacancy engineering offers an alternative route to aliovalent and interstitial doping for optimization of the carrier concentration in thermoelectric materials. For the wide-bandgap semiconductor $BaCu_2Se_2$, the Cu vacancy is dynamically stable; this feature can be rationally manipulated to maximize the thermoelectric figure of merit zT. In this work, we show that at room temperature, Cu-deficient $BaCu_{2-x}Se_2$ samples exhibit increased hole effective mass and mobility, attributed to the energy band modulation, which are favorable for improved electrical transport properties. More importantly, the defect energy level resulting from the Cu vacancies continually contributes holes at high temperature, thereby allowing the hole concentration to approach an optimal concentration. This effect leads to an increase of the power factors over a wide temperature range. The artificial reduction of the Cu content in $BaCu_2Se_2$ results in the strengthened point-defect scattering, suppressing the lattice thermal conductivity. This strategy allows simultaneous optimization of the electrical and thermal transport properties, with a thermoelectric figure of merit $zT = 1.08$ achieved for $BaCu_{1.94}Se_2$ at 823 K, which is 38% higher than that of stoichiometric $BaCu_2Se_2$. Within the measured temperature range, the average zT value for $BaCu_{1.94}Se_2$ is 0.494, which is 52.9% higher than that of $BaCu_2Se_2$.

1. Introduction

Thermoelectric (TE) materials, which can be used to convert a temperature gradient into electricity based on the Seebeck effect, have important applications ranging from recycling waste heat to powering space-exploration missions [1]. The performance of a TE material is determined by its dimensionless figure of merit, $zT = \sigma S^2 T/\kappa$, where T is the operating temperature in Kelvin, and σ, S, and κ are the electrical conductivity, Seebeck coefficient, and thermal conductivity (including the lattice thermal conductivity κ_L and electronic thermal conductivity κ_e), respectively [2]. Ideal high-performance TE materials require both excellent electrical transport properties (evaluated by the power factor $PF = \sigma S^2$) and low thermal conductivities. However, the strong coupling among σ, S, and κ_e related to the carrier concentration leads to great difficulties in obtaining a high zT [3,4].

The concept of "Phonon-Glass, Electron-Crystal" (PGEC) was proposed in 1995 by Slack [5], which implies that the state-of-the-art TE compounds would possess excellent electrical transport properties like crystals and low thermal conductivity like glasses. This idea guided material scientists to explore filled-skutterudite as the first successful example, where filled atoms act as phonon-scattering centers while the $CoSb_3$ framework is responsible for the charge transport [6]. Recently, Zintl phases have been reported as an emerging TE materials that meet the requirements of PGEC, mainly because of the roles played by the Zintl cations and anions [7–9]. Specifically, the polyanion frameworks provide electronic tunnels through the covalently bonded network of complex metals or metalloids. In addition, diverse and anisotropic chemical bonding leads to strong lattice anharmonicity, which explains

* Corresponding authors.
E-mail addresses: kai.guo@gzhu.edu.cn (K. Guo), lilyxi@t.shu.edu.cn (L. Xi), yjiang0209@t.shu.edu.cn (Y. Jiang).
[1] These authors contributed equally to this work.

https://doi.org/10.1016/j.cej.2022.135302
Received 4 November 2021; Received in revised form 10 February 2022; Accepted 13 February 2022
Available online 16 February 2022

the low lattice thermal conductivity typically observed in Zintl compounds [10]. In particular, layered 122-type Zintl phases, such as $EuZn_2Sb_2$ [11], $YbCd_2Sb_2$ [12,13], $CaMg_2Bi_2$ [14], and $YbZn_2Sb_2$ [15], have attracted extensive attentions in recent years, and caged 122-type Zintl phases with the orthorhombic structure have occasionally been discussed as TE candidates. Our group revealed the TE potential of orthorhombic $BaCu_2Te_2$, which processes an intrinsically high hole concentration at room temperature due to the thermodynamically stable Cu vacancies [16,17]. Thus, Ag doping and Cu compensation have been intentionally performed aiming to suppress exorbitant Cu vacancies, which is beneficial for the optimization of the hole concentration and improvement of the power factor.

Orthorhombic α-$BaCu_2Se_2$ [18], isostructural to $BaCu_2Te_2$, consists of a cage-like three-dimensional network of Cu and Se atoms with two local tetrahedral environments, regular and distorted respectively, for the centered Cu atoms. The corner- and edge-sharing tetrahedrons play an important role in the carrier transport, whereas the heavy-atom Ba is viewed as the phonon-scattering center. Zhao et al. reported that the heavy doping of Na at Ba sites in $BaCu_2Se_2$ can transform the orthorhombic $BaCu_2S_2$ type (*Pnma*) into a tetragonal $ThCr_2Si_2$ type (*I4/mmm*) [19]. Unlike $BaCu_2Te_2$, the intrinsic carrier concentration of α-$BaCu_2Se_2$ is too low to reach the optimal carrier concentration of high-performance TE compounds (10^{19}–10^{20} cm^{-3}) [20,21], which is the key factor limiting its TE properties.

Aliovalent doping in the single-phase region is a simple but effective way to control and optimize the carrier concentration [22]. In principle, the optimal value of the carrier concentration for a specific TE material is temperature dependent [23]. Thus, simple manipulation would not realize the dynamic effect in heavily doped semiconductors [24,25]. In this paper, we propose Cu vacancy engineering in $BaCu_2Se_2$, with the aim of optimizing the hole concentration and improving the TE performance. The results indicate that at room temperature, the hole concentration increases by an order of magnitude and that both the effective mass and mobility are enhanced due to energy-band modulation with the increase of Cu vacancies. Notably, the defectenergy levels of the Cu vacancies in all the samples lead to a continuous rise of the carrier concentration over a wide temperature range, which approaches the optimal carrier concentration obtained by calculation and fitting. Combined with the improved power factor and suppressed thermal conductivity resulting from the point defects, a competitive zT of 1.08 was achieved for $BaCu_{1.94}Se_2$ at 823 K. Meanwhile, the average zT value of $BaCu_{1.94}Se_2$ is 0.494 within the temperature range of 300–823 K, which is 52.9% greater than that of pristine $BaCu_2Se_2$.

2. Experimental section

2.1. Sample synthesis

Polycrystalline $BaCu_{2-x}Se_2$ ($x = -0.02$, 0, 0.02, 0.04, 0.06) samples were directly synthesized from the corresponding elements by solid-state reaction method. The raw materials Ba blocks (99.9%), Cu sheets (99.999%) and Se powders (99.999%) were weighed according to the stoichiometric ratio, and then loaded into a glass-carbon crucible within an argon-filled glove box ($H_2O < 0.1$ ppm, $O_2 < 0.1$ ppm, MBRAUN). These assembles were sealed into a quartz tube, transferred to a muffle furnace for heating at 723 K over 10 h, followed by further annealing at 973 K at a heating rate of 20 K/h and held for another 36 h. In order to obtain homogeneous samples, the products were ground into powder in the glove box, and underwent an annealing treatment at 827 K for 24 h. The as-obtained samples were ground into powder again, loaded into a graphite die with the diameter of Φ10 mm, sintered and densified in a vacuum hot-pressing furnace. The sintering pressure and temperature were set as 65 MPa and 823 K (30 min), respectively. The real densities of the hot-pressed samples were more than 97% compared with the theoretical density, as showed in Table S1.

2.2. Sample characterization

The phase structures of as-obtained samples were studied by powder X-ray diffraction (PXRD, D/max-2200, Rigaku, Cu Kα radiation, 10° ~ 90°, Japan) technology. The lattice parameters were calculated using Fullprof software [26]. In order to understand the lattice dynamics of $BaCu_2Se_2$, the temperature-variable X-ray diffraction measurements (Rigaku SmartLab SE) from room temperature to 1073 K were carried out. The microstructure and composition homogeneity were examined by scanning electron microscope (SEM; ZEISS Gemini SEM300) and energy dispersive X-ray spectroscopy (EDS) system, respectively. The atomic structure of polycrystalline samples was characterized by spherical aberration corrected transmission electron microscope (TEM; Themis ETEM, Thermo Fisher Scientific, USA). Prior to the observation, the sample was prepared with a focused ion beam (FIB) system. The Seebeck coefficients and electrical conductivities were synchronously collected using a ZEM-3 instrument (ULVAC-RIKO, Japan) under a helium atmosphere. The thermal conductivities were calculated using the formula $\kappa = C_p\ \lambda\ \rho$, where λ is the thermal diffusivity measured in an argon atmosphere using the laser flash diffusivity method (LFA 467HT, Netzsch). The densities (ρ) for the bulk materials were obtained from the Archimedes principle. The specific heat (C_p) was achieved by both theoretical estimation (Dulong-Petit law) and experimental measurement (differential scanning calorimetry, STA 449F3, Netzsch, Fig. S1). The Hall coefficient (R_H), mobility (μ) and carrier concentration (p) were measured by 8400 series HMS system with a reversible magnetic field of 0.9 T (Lake Shore Cryotronics). The values of band gaps were extracted by the diffuse reflectance model with a Hitachi u4150 UV–vis-NIR spectrophotometer (Japan). The sound velocity of the sample is tested by UMS-100 (Ultrasonic Echometer, France).

2.3. Energy band and defect formation energy calculation

The total energy and band structure calculations were performed by the projector augmented wave (PAW) method as implemented in Vienna ab initio Simulation Package (VASP) package [27–29]. To obtain the accurate band gap, The Heyd-Scuseria-Ernzerhof (HSE) hybrid functional was employed as the exchange–correlation functional in band structure calculations [30]. The HSE screening parameter was set to 0.2 $Å^{-1}$. During defect-energies calculations, the exchange and correlation energy we used was approximated by generalized gradient approximation (GGA) under the scheme of Perdew-Burke-Ernzerhof (PBE) [31], and the Coulomb (U) [32] was introduced within the GGA + U model. Ueff, set to 4 eV, was added to the *d* orbital of the Cu element. For the calculations of formation energy of defects in $BaCu_2Se_2$, we adopted the supercell structure of 2*3*2 (240 atoms) and the *k*-mesh [33] was 1*1*1. The lattice constants and ionic positions of the structures without defects were fully relaxed within energy convergence criterion of 10^{-4} eV, while the supercells containing defect only relaxed the ionic position. The cutoff energies of plane-wave were both set as 380 eV during all calculations.

3. Results and discussion

According to previous reports, $BaCu_2Se_2$ has orthorhombic (α-phase) and tetragonal (β-phase) structures. Normally, $BaCu_2Se_2$ is stable in the orthorhombic phase, whereas heavy p-doping would transform the α-phase into the β-phase [34]. Fig. 1a presents the crystal structure of orthorhombic α-$BaCu_2Se_2$ and tetragonal β-$BaCu_2Se_2$. In the former, four Se atoms are centered on Cu atoms to form a $CuSe_{4/4}$ tetrahedron and form a column along the *b* direction through edge sharing. These columns are connected by a common corner to generate the three-dimensional frame, playing a vital role in hole transport [35]. Ba atoms fill in the cages as chains along the *b*-axis. The size of the cage (the maximum and the minimum distances are 8.9 and 2.62 Å, respectively) is much larger than the radius of Ba ions (1.35 Å), which may result in

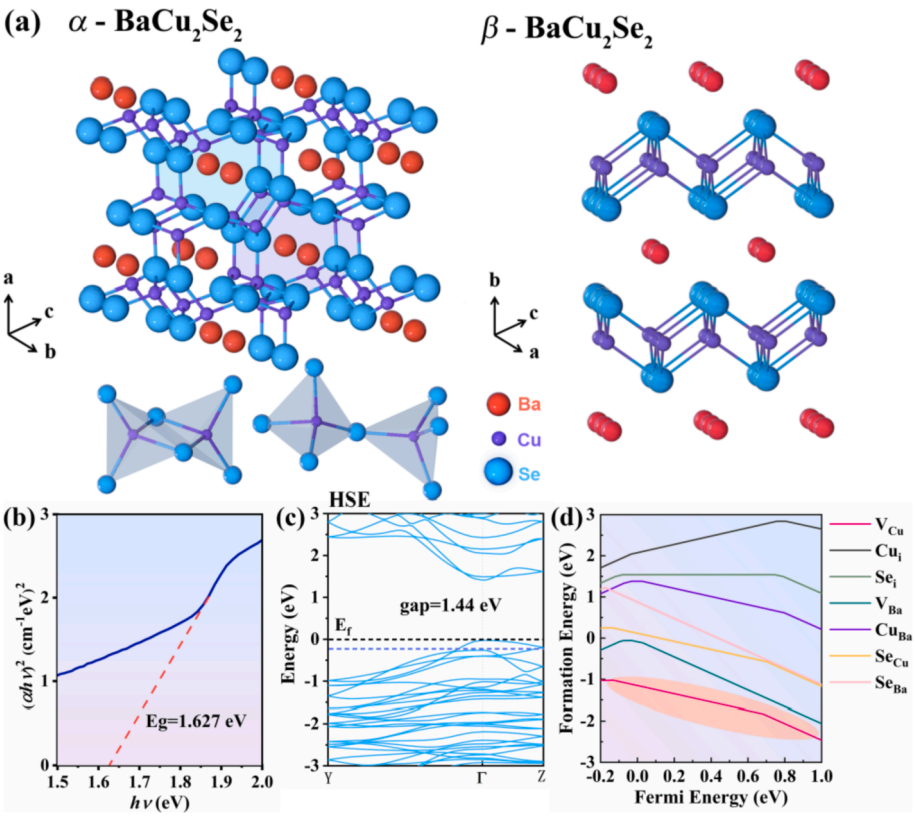

Fig. 1. (a) Crystal structure of α-$BaCu_2Se_2$ and β-$BaCu_2Se_2$, (b) the optical band gap of pristine $BaCu_2Se_2$ deduced from the absorption spectra using the Kubelka-Munk relation, (c) band gap of $BaCu_2Se_2$ calculated using the HSE method, and (d) calculated defect formation energy E_{form} in $BaCu_2Se_2$ as a function of Fermi energy for Cu-poor and Se-rich condition, clearly indicating that the Cu vacancy is the most stable defect.

low lattice thermal conductivity because of the weak binding interactions. According to our experimentally determined value of 1.627 eV (Fig. 1b), α-$BaCu_2Se_2$ is a wide-bandgap semiconductor, as also evidenced by the calculated electronic band structures using the HSE approaches along the high-symmetry directions (Fig. 1c). $BaCu_2Se_2$ has a direct band gap of 1.44 eV, which is close to the calculated value determined by Zou et al. [36] using the HSE method. Generally, most superior TE materials are narrow-band-gap semiconductors, including PbTe [37], Sb_2Te_3 [38], Bi_2Te_3 [39], and Mg_3Sb_2 [40]. Wide-bandgap semiconductors are often overlooked in the TE community because of their poor electrical properties, which is attributed to their inherently low carrier concentration. However, wide band gaps can suppress the bipolar diffusion and favor a high working temperature, opening the way for a new TE research field [41].

In principle, instinct defects exist in semiconductors for thermodynamic reasons, which also essentially determined the conduction behaviors. Herein, the defect formation energy (E_f^d) was calculated to reveal the potential instinct defects in α-$BaCu_2Se_2$ using the following equation [42]:

$$E_f^d = E_{tot}^d(defect) - E_{tot}^p(perfect) - \Sigma_i n_i \mu_i + q(E_f + E_v + \Delta V) \quad (1)$$

where $E_{tot}^d(defect)$ and $E_{tot}^p(perfect)$ are the total energy of defect structures and perfect structures, respectively; n_i is the number of atoms of the i-th type (host or impurity atoms) added to (n_i greater than 0) or deleted from ($n_i < 0$) the matrix; μ_i is the chemical potential; q is the charge state of the defect; E_f is the Fermi level with respect to the valence band maximum (E_v) of the bulk system; and ΔV is the electrostatic potential difference between the perfect system and the defective system. The formation energy of the Cu vacancies was the lowest (Fig. 1d), suggesting that V_{Cu} defects can be easily formed during the synthesis processes, which demonstrates that α-$BaCu_2Se_2$ is a p-type conductive material according to the following defect-reaction equation:

$$Ba^{2+}(Cu_2Se_2)^{2-} \rightarrow Ba^{2+}(Cu_{2-x}Se_2)^{(2+x)-} + xCu^0 + xh^+ \quad (2)$$

To improve the TE performance of wide-bandgap p-type materials, it is key to increase the carrier concentration to an optimum level. The experimental hole concentration of pristine $BaCu_2Se_2$ is $\sim 3.2 \times 10^{18}$ cm^{-3}, which largely deviates from the optimal carrier concentration corresponding to the maximum power factor. Because this limitation of natural Cu vacancies prevents the power factor from being maximized, artificial reduction of the Cu content was performed to enhance the electrical transport properties.

In fact, the increase of Cu vacancies not only increases the originally insufficient carrier concentration but also promotes the downward shift of the Fermi level [43], leading to a high possibility of reaching the second valence band (Fig. 1c). In this case, the hole effective mass may be enhanced. Moreover, the defect energy level formed by the Cu vacancy defect can release the potential mechanism of excited carriers in α-$BaCu_2Se_2$ [44]; that is, the defect energy level can continuously excite the carriers at high temperature, which can result in an appropriate carrier concentration over the entire temperature range. A detailed discussion is provided in the following section. Therefore, Cu vacancy engineering in α-$BaCu_2Se_2$ enables optimization of the carrier concentration by artificially reducing the Cu content.

To reveal the effect of Cu vacancies on the TE performance of α-$BaCu_2Se_2$, pristine and Cu-deficient $BaCu_{2-x}Se_2$ ($x = -0.02, 0, 0.02, 0.04, 0.06$) samples were synthesized and the PXRD results at room temperature are presented in Fig. 2a. The main diffraction pattern of these polycrystalline samples can be indexed as the orthorhombic $BaCu_2S_2$ structure with space group *Pnma*. The diffraction peaks gradually shifted to a higher angle upon decreasing the Cu content, indicating that the lattice parameters *a*, *b*, and *c* shrink as *x* increases (Fig. S2). Fig. 2b and Table S2 show the dependence of the lattice

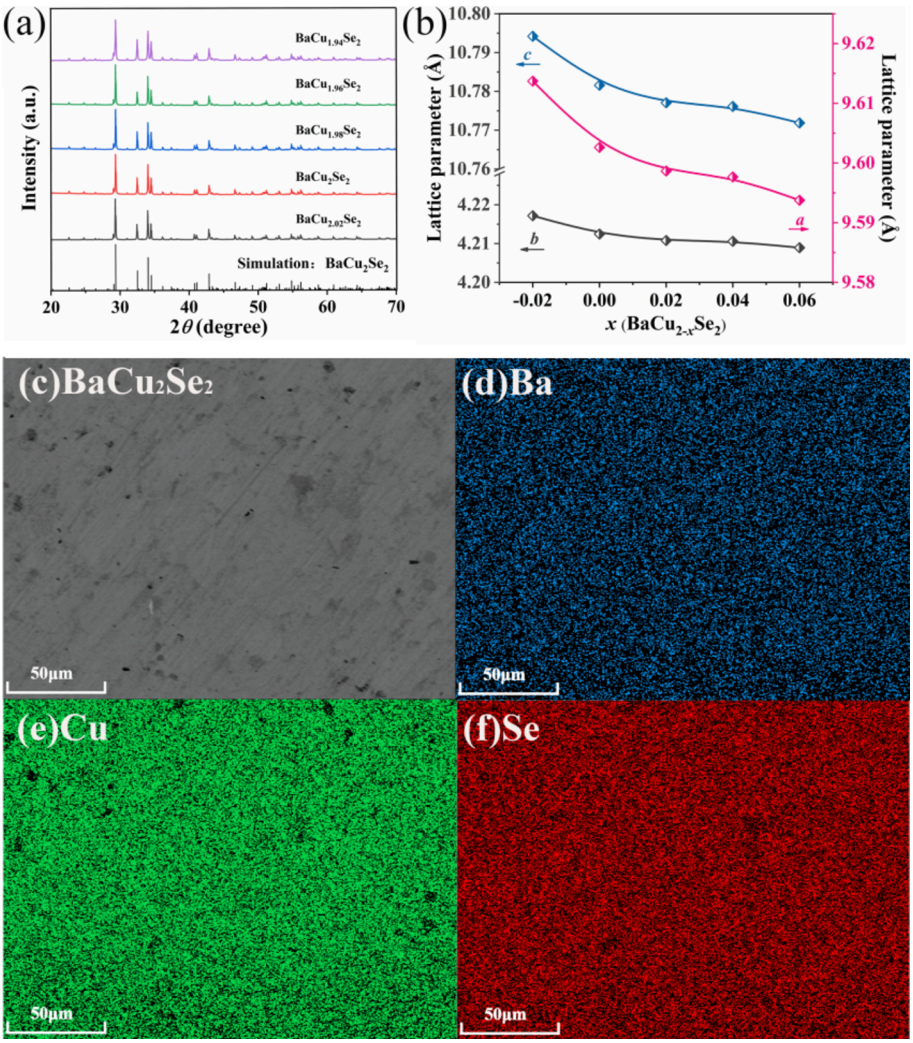

Fig. 2. (a) Powder XRD patterns and (b) lattice parameters of $BaCu_{2-x}Se_2$ ($x = -0.02$, 0, 0.02, 0.04, 0.06) samples. (c) SEM images of $BaCu_2Se_2$. (d–f) EDS maps corresponding to the rectangular area of $BaCu_2Se_2$.

parameters in three directions on the Cu content, with all three parameters monotonously decreasing. In addition, the change of the lattice parameter in the *b*-axis is weakly correlated to the other two because it is mainly determined by the Ba cation chains.

To further demonstrate the purity and uniformity of the sample, SEM observations and corresponding EDS measurements were made for the $BaCu_2Se_2$ sample. Fig. 2c presents back scattered-electron images of a typical $BaCu_2Se_2$ sample. A small amount of micropores can be observed, which appear as black dots and are consistent with the real density (Table S1). EDS mapping indicates that Ba, Cu, and Se were uniformly distributed in samples (Fig. 2d–f) with a small trace of copper selenide distributed along the grain boundaries (Fig. S3 and Table S3).

Fig. 3a shows the calculated carrier-concentration-dependent *S*, $S^2\sigma$, and zT at room temperature. The results indicate that the optimal carrier concentration corresponding to the maximum *PF* is 6.3×10^{19} cm^{-3} at room temperature, which is much higher than the experimental value for pristine $BaCu_2Se_2$ (3.2×10^{18} cm^{-3}) (Fig. 3b). By intentionally introducing holes through vacancy engineering, a great increase of up to 2.81×10^{19} cm^{-3} can be realized, which is close to the optimal carrier concentration. In addition, the hole mobility also undergoes a modest rise with increasing Cu vacancy concentration at 300 K, reaching a peak at $x = 0.04$. By applying the single parabolic band (SPB) model with the assumption of acoustic phonons dominating the charge transport [45], the Pisarenko lines at 300 K are plotted in Fig. 3c. The effective masses of Cu-deficient $BaCu_{2-x}Se_2$ samples are clearly larger than that of the pristine sample, indicating that the reduction of the Cu content increases the effective mass. This result can be understood from the involvement of the second valence band. The higher carrier concentration can activate the second valence bands participating in the hole transport to enhance the effective mass. The TEM image demonstrates the good crystallization of the sample, and it corresponds well to the [-1 1 -1] projection of α-$BaCu_2Se_2$ (Fig. 3d).

Furthermore, to verify the presence of Cu vacancies within the sample, a spherical-aberration-corrected transmission electron microscope was used to characterize the atomic configuration. Fig. 4a displays a typical high-angle annular dark-field (HAADF) image of $BaCu_{1.94}Se_2$, projected along the [0 1 0] direction according to the selected area electron diffraction (SAED) pattern inset. The diffraction spots indicate the interplanar distances of 10.16 Å and 11.65 Å, agreeing well with that of (1 0 0) and (0 0 1) of $BaCu_2Se_2$, respectively. As the all know, the contrast in the HAADF image is highly dependent on the atomic number, the region with dark contrast (marked by the yellow dashed rectangle) is deduced to be atom-deficient.

Fig. 4b shows the electron energy loss spectroscopy (EELS) spectrum extracted from the orange line (Fig. 4a), which indicates the constituent elements of Ba, Cu, and Se. The variation of the chemical composition across the dark-contrast region in the direction of the arrow is explored by the line profile in Fig. 4c, where there is a dramatic drop in the intensity of Cu compared with that of the Ba and Se elements. The Cu deficiency or vacancies are further confirmed by the atom-resolved

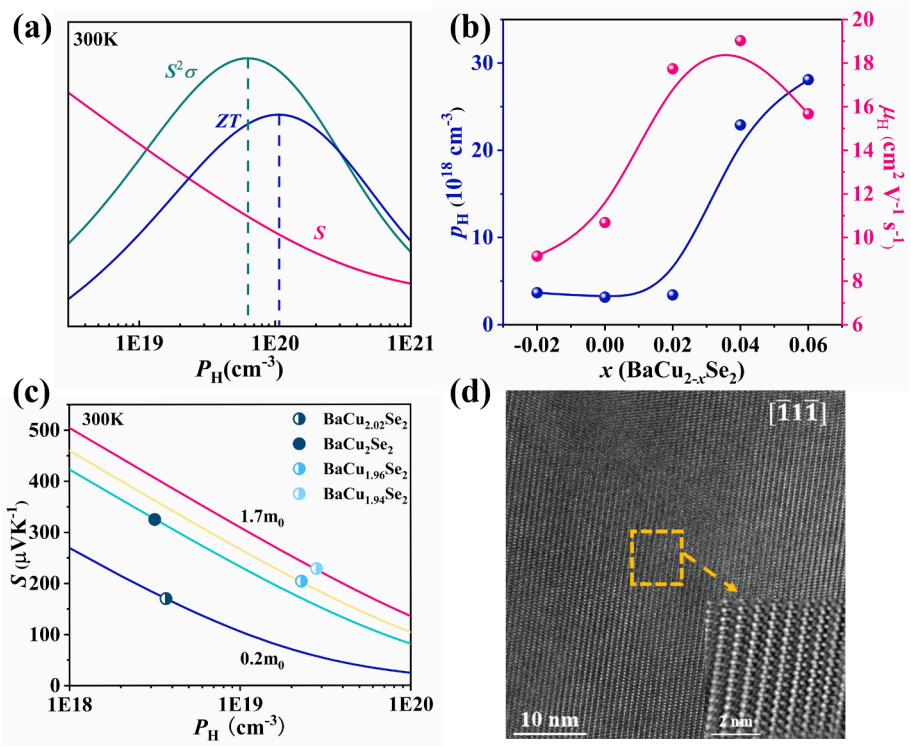

Fig. 3. (a) Calculated S, $S^2\sigma$, and zT as a function of hole concentration at 300 K; (b) experimental carrier concentration and mobility depending on Cu content at 300 K; (c) Pisarenko lines at 300 K; (d) TEM image of $BaCu_{1.94}Se_2$, which indicates good crystallinity.

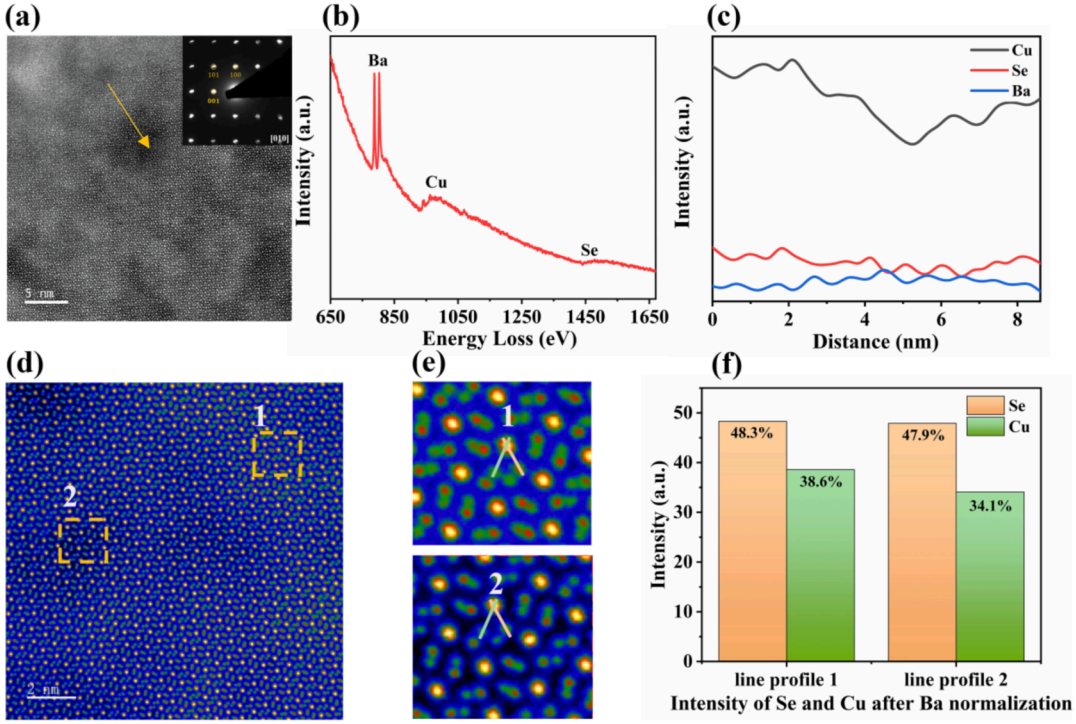

Fig. 4. (a) HAADF image of $BaCu_{1.94}Se_2$ with SAED pattern inset, (b) EELS spectrum extracted from the orange line, (c) intensities of Ba, Cu and Se along the direction marked by the arrow, (d and e) HAADF images showing two different contrast areas [1,2], and (f) intensity of Se and Cu after Ba normalization.

HAADF image in Fig. 4d. According to the crystalline structure of $BaCu_2Se_2$, single-type atom columns can be observed along the [0 1 0] zone axis. Therefore, the brightest atom columns in Fig. 4d correspond to Ba ($Z = 56$), the middle-level ones to Se ($Z = 34$), and the lowest ones to Cu ($Z = 29$). After Ba normalization, the relative intensities of the Cu and Se columns for the normal region (region 1) and atom-deficient region (region 2) were extracted, as shown in Fig. 4e–f. This result indicates almost no change of Se but a dramatic lack of Cu. The above evidence indicates the presence of Cu vacancies in the lattice.

To verify the thermal stability and lattice dynamics of α-$BaCu_2Se_2$,

variable temperature X-ray diffraction measurements from room temperature to 900 K were conducted (Fig. 5a). No prominent phase transition was observed during the heating process. Aside from the diffraction shift, all the patterns remained unchanged over the test temperature, as shown in Fig. S4. The low-angle shift of the diffraction peak from the enlarged image corresponds to the normal thermal expansion behavior of $BaCu_2Se_2$. The lattice parameters calculated from the refined X-ray diffraction pattern uniformly increased along the three axes (*a*-, *b*-, *c*-) during the heating process, indicating weak anisotropy.

Fig. 5b–d show the temperature dependences of electrical conductivity, Seebeck coefficient and power factor for the $BaCu_{2-x}Se_2$ ($x = -0.02$, 0, 0.02, 0.04, 0.06) samples from 300 K to 823 K. The electrical conductivity was greatly improved with increasing x from 4.53 S cm^{-1} for the pristine sample to 73.7 S cm^{-1} for $BaCu_{1.96}Se_2$ at room temperature, which is attributed to the increase of both the hole concentration and mobility (Fig. 5b). The electrical conductivities of $BaCu_2Se_2$ and $BaCu_{2.02}Se_2$ exhibit semiconductor behavior from room temperature to 723 K, with their electrical conductivities increasing monotonically with increasing temperature. However, the electrical conductivity of the Cu-deficient samples gradually decreased before the critical point of 500 K and then remarkably increased as the temperature increased to 700 K because of the rise of the hole concentration. The activation energy can be determined by fitting the curve of the electrical conductivity as a function of temperature from 500 K to 700 K (Fig. S5), which basically shows a decreasing trend. Considering the large value of the activation energy, the holes form impurity level cannot be fully excited at room temperature (Fig. 6). With increasing of Cu vacancies, the activation energy gradually decreases, indicating that the holes can be generated at lower temperature for Cu-deficient samples in comparison with the pristine $BaCu_2Se_2$. Hence, the carrier concentration of the Cu-deficient samples rises slightly in the low temperature region, and after 500 K, the holes are gradually activated as the temperature rises, which is responsible for the continuously increasing σ, accounting for the unusual σ–T behavior of the $BaCu_{2-x}Se_2$ ($x = 0.02$, 0.04, 0.06) samples.

As shown in Fig. 5c, the positive values of the Seebeck coefficient indicate p-type conduction. The Seebeck coefficients are in the measured temperature range from 200 to 300 μV K^{-1}, which are suitable for TE considerations. In addition, the Seebeck coefficient declines from ~ 325 μV K^{-1} for $BaCu_2Se_2$ to ~ 204 μV K^{-1} for $BaCu_{1.96}Se_2$ at room temperature, which is attributed to the higher hole concentration of $BaCu_{1.96}Se_2$. The behavior of the Seebeck coefficients with temperature

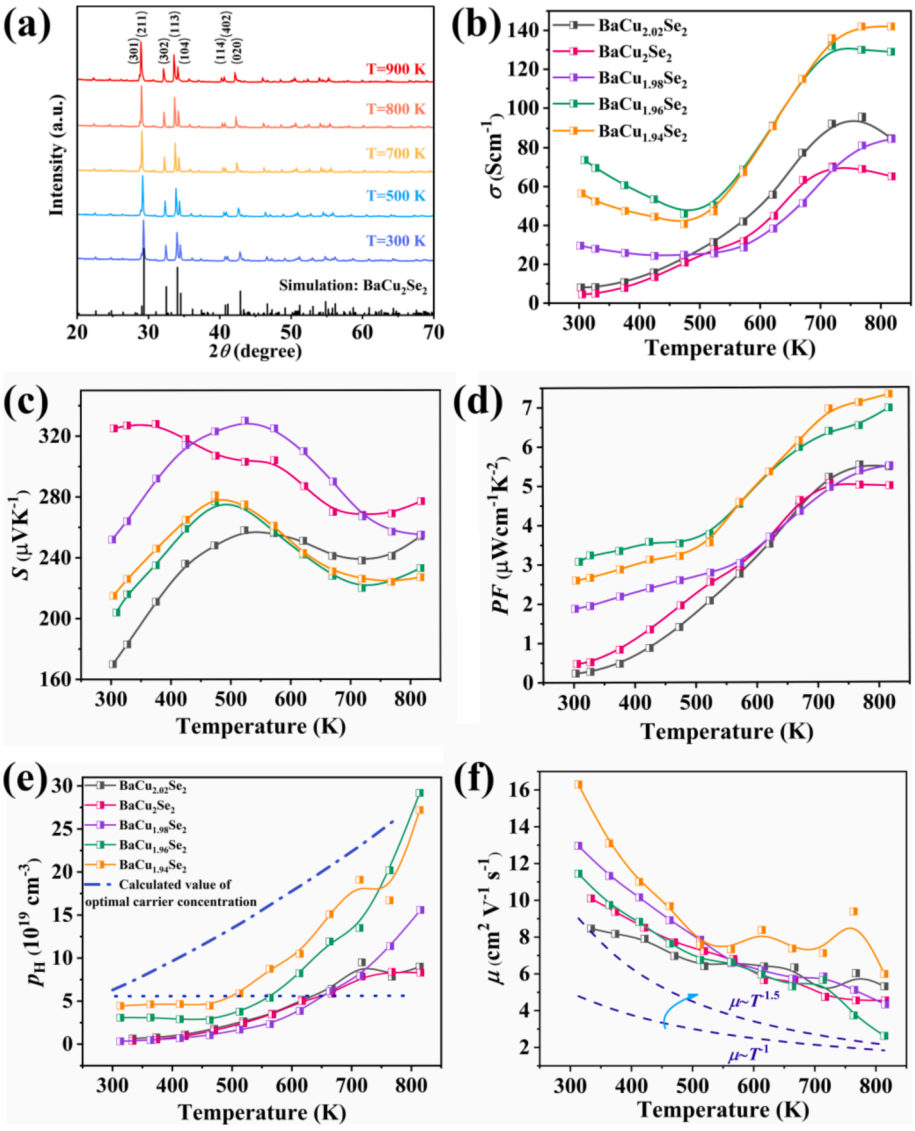

Fig. 5. (a) Variable temperature XRD patterns of $BaCu_2Se_2$, temperature dependence of (b) electrical conductivity, (c) Seebeck coefficient, (d) power factor, (e) carrier concentration, and (f) carrier mobility of $BaCu_{2-x}Se_2$ ($x = -0.02$, 0, 0.02, 0.04, 0.06).

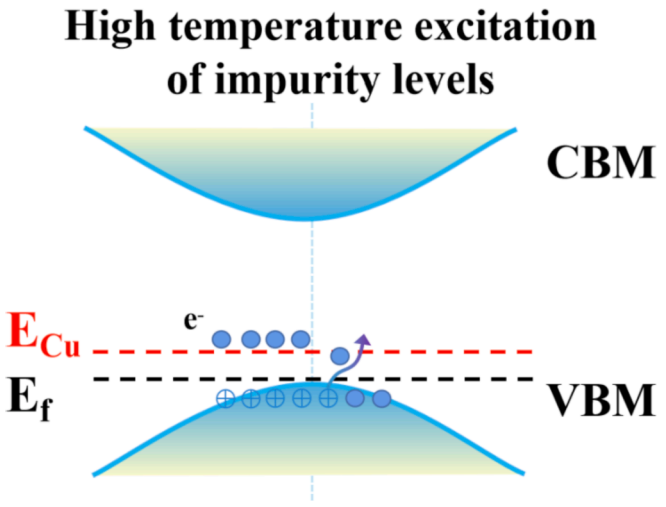

Fig. 6. The Cu defect level is excited at high temperature, which leads to a continuous increase of the carrier concentration.

can be roughly understood from the $S \sim [\pi/(3n)]^{2/3} m^* T$ relation. The upward trend at low temperatures is attributed to the increase of the effective mass, while the sharp increase in the carrier concentration after 473 K can result in the rapid decrease of the Seebeck coefficients. The *PF* values show a monotonous growth with increasing temperature and Cu vacancies over the entire temperature range, which is due to the continuous increase of the carrier concentration. Consequently, the *PF* values are enhanced dramatically, up to 544% at room temperature, with a peak value of 7.33 μW cm^{-1} K^{-2} at 823 K achieved for $BaCu_{1.94}Se_2$, which is an increase of 40% compared with that of the pristine sample (Fig. 5d).

It is easy to tune the hole concentration to an optimal value at a certain temperature; however, maintaining the optimum value within the measured temperature range is very difficult. Previously, Luo's group used the dynamic doping effect on PbSe and PbS, enabling the carrier concentration to remain close to the optimal value over a wide temperature range [46,47]. A similar effect occurs in $BaCu_{2-x}Se_2$, as shown in Fig. 5e. The hole concentration of $BaCu_{2-x}Se_2$ exhibits an abnormal temperature-dependent behavior, continuously increasing with increasing temperature. This behavior can be understood from the continuous excitation of carriers by the Cu-defect energy level (Fig. 6). The electrons at the valence band maximum (VBM) are continually excited to the impurity level at high temperature, which leads to the increase of hole concentration involved in conduction. The experimental hole concentration data for $BaCu_{1.94}Se_2$ approximately fits the curve of the calculated data. Besides, the mobility of all the samples, as shown in Fig. 5f, decreases slightly with temperature. It should be noted that with decreasing Cu content, the dependence of the carrier mobility on the temperature changed from T^{-1} to $T^{-1.5}$ after careful fitting (dashed line in Fig. 5f), which indicates that there is not a single scattering mechanism and a possible combination of alloying and acoustic phonon scattering mechanisms. As the Cu content decreases, the acoustic phonon scattering mechanism plays a more dominant role.

As shown in Fig. 7a, the total thermal conductivity of α-$BaCu_2Se_2$ decreases from 1.06 to 0.53 W m^{-1} K^{-1} upon increasing the temperature from 303 K to 823 K, demonstrating that α-$BaCu_2Se_2$ is a compound with intrinsically low thermal conductivity. In addition, the introduction of Cu vacancies further reduces the thermal conductivity. To understand the effect of Cu vacancies on the thermal transport properties, we calculated the electronic thermal conductivity κ_e using the Wiedemann–Franz law, $\kappa_e = L\sigma T$ (Fig. 7 b). The lattice thermal conductivity κ_L is estimated by subtracting the electronic κ_e from the total thermal conductivity (Fig. 7c). *L* is the Lorenz factor determined from the above SPB model with acoustic phonon scattering from the total thermal conductivity. As we can see, the lattice thermal conductivity decreases slightly with increasing Cu vacancy concentration because of the scattering of point defects. As the temperature increases, κ_L roughly obeys a T^{-1} relationship, which can be attributed to Umklapp processes being predominant at elevated temperatures. The lowest κ_L at room temperature is 0.83 W m^{-1} K^{-1} for composition $BaCu_{1.94}Se_2$ at room

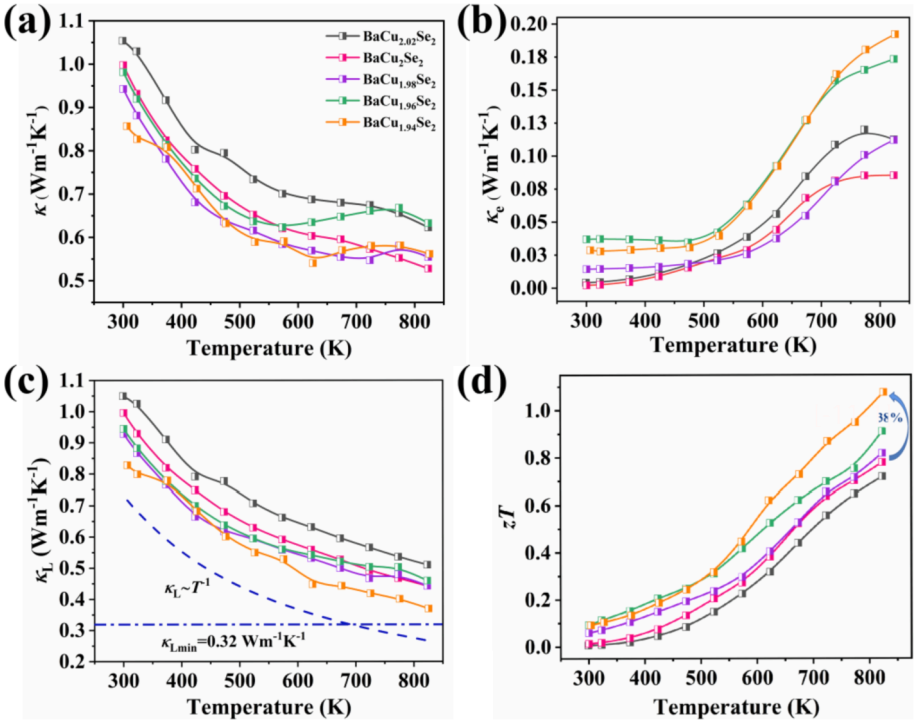

Fig. 7. Temperature dependence of (a) total thermal conductivity, (b) electronic thermal conductivity, (c) lattice thermal conductivity, and (d) dimensionless figure of merit of $BaCu_{2-x}Se_2$ ($x = -0.02$, 0, 0.02, 0.04, 0.06).

temperature, which is comparable to that of other TE materials with intrinsically low thermal conductivity [48,49]. The limiting of the lattice thermal conductivity of $BaCu_2Se_2$ can be evaluated using the following equation [50] by applying the measured sound velocity (Table S4), as shown in Fig. S6, which is approximately 0.32 W m^{-1} K^{-1} in the temperature range. Distinctly, there is room for the thermal conductivity to drop, and further exploration experiments can be performed to enhance the TE properties.

$$\kappa_{min} = \frac{k_B}{2\pi v_s}\left(\frac{k_B T}{\hbar}\right)^2 \int_0^{\theta_D/T} \frac{x^3 e^x}{(e^x-1)^2} dx \quad (3)$$

Combining the relatively stable inherent thermal properties of the material and improved electrical properties due to the optimization of the carrier concentration, an improved zT was obtained. Fig. 7d shows that the zT values increase with increasing temperature, with a maximum zT of 1.08 achieved at 823 K for $BaCu_{1.94}Se_2$, which is 38% higher than that of $BaCu_2Se_2$. The average zT of $BaCu_{1.94}Se_2$ is 0.494 within the entire temperature range, which is higher by 52.9% than that of the pure sample. The zT value could be further enhanced through optimization of the carrier concentration and reduction of the thermal conductivity. These results indicate that the wide-bandgap semiconductor $BaCu_2Se_2$ can be used as a promising p-type TE material, and vacancy engineering provides an effective route to improve the TE properties of wide-bandgap semiconductors.

4. Conclusions

Vacancy engineering is a successful strategy to optimize the electrical and thermal transport properties in TE investigation. In this work, Cu vacancies were intentionally introduced to manipulate the hole concentration of wide-bandgap α-$BaCu_2Se_2$. Combining the experimental work with calculation results, the optimal hole concentration could be realized at room temperature for Cu-deficient samples. In addition, the defect energy level of Cu vacancies can contribute extra holes at high temperature, which enables the real hole concentration approach to the optimal one, signifying an improvement of the power factor within a broad temperature range. The point-defect scattering was strengthened from the lack of Cu, which favors the reduction of the lattice thermal conductivity. An enhanced zT of 1.08 was achieved at 823 K for $BaCu_{1.94}Se_2$, which is 38% higher than that of pristine sample at the same temperature. The space of tuning the hole concentration to the optimal one and reducing the lattice thermal conductivity approaching to the glass limit allows to further enhancement of TE properties in α-$BaCu_2Se_2$.

Declaration of Competing Interest

The authors declare that they have no known competing financial interests or personal relationships that could have appeared to influence the work reported in this paper.

Acknowledgment

This work was financially supported by the National Key Research and Development Program of China (2018YFA0702100), the National Natural Science Foundation of China (21771123, 52072234 and U21A2054), the Open Project of Jiangsu Key Laboratory for Carbon-Based Functional Materials & Devices (KJS2023). J. Jiang acknowledges the support from Shanghai Technical Service Center for Advanced Ceramics Structure Design and Precision Manufacturing (NO. 20DZ2294000).

Appendix A. Supplementary data

Supplementary data to this article can be found online at https://doi.org/10.1016/j.cej.2022.135302.

References

[1] J. He, T.M. Tritt, Advances in thermoelectric materials research: Looking back and moving forward, Science 357 (2017) 1–9. https://www.science.org/doi/10.1126/science.aak9997.
[2] L.D. Zhao, S.H. Lo, Y.S. Zhang, H. Sun, G.J. Tan, C. Uher, C. Wolverton, V. P. Dravid, M.G. Kanatzidis, Ultralow thermal conductivity and high thermoelectric figure of merit in SnSe crystals, Nature 508 (7496) (2014) 373–377. http://www.nature.com/doifinder/10.1038/nature13184.
[3] G.J. Tan, L.D. Zhao, M.G. Kanatzidis, Rationally Designing High-Performance Bulk Thermoelectric Materials, Chem. Rev. 116 (19) (2016) 12123–12149. https://doi.org/10.1021/acs.chemrev.6b00255.
[4] M.W. Gaultois, T.D. Sparks, C.K. Borg, R. Seshadri, W.D. Bonificio, D.R. Clarke, Data-driven review of thermoelectric materials: performance and resource considerations, Chem. Mater. 25 (15) (2021) 2911–2920. https://doi.org/10.1021/cm400893e.
[5] G.A. Slack, New materials and performance limits for thermoelectric cooling, CRC Handb. Thermoelectr. (1995) 407–440.
[6] X. Shi, J. Yang, J.R. Salvador, M.F. Chi, J.Y. Cho, H. Wang, S.Q. Bai, J.H. Yang, W. Q. Zhang, L.D. Chen, Multiple-filled skutterudites: high thermoelectric figure of merit through separately optimizing electrical and thermal transports, J. Am. Chem. Soc. 133 (20) (2011) 7837–7846. https://doi.org/10.1021/ja111199y.
[7] F. Gascoin, S. Ottensmann, D. Stark, S.M. Haïle, G.J. Snyder, Zintl phases as thermoelectric materials: tuned transport properties of the compounds $Ca_xYb_{1-x}Zn_2Sb_2$, Adv. Funct. Mater. 15 (11) (2005) 1860–1864. https://doi.org/10.1002/adfm.200500043.
[8] X. X. Yang, Y. Y. Gu, Y. P. Li, K. Guo, J. Y. Zhang, J. T. Zhao, The equivalent and aliovalent dopants boosting the thermoelectric properties of $YbMg_2Sb_2$, Sci. China Mater. 63 (3) (2020) 437-443, https://dx.doi.org/10.1007/s40843-019-1199-4.
[9] E.S. Toberer, A.F. May, G.J. Snyder, Zintl chemistry for designing high efficiency thermoelectric materials, Chem. Mater. 22 (3) (2010) 624–634. https://doi.org/10.1021/cm901956r.
[10] K. Guo, T. Weng, Y. Jiang, Y. Zhu, H. Li, S. Yuan, J. Yang, J. Zhang, J. Luo, Y. Grin, J.-T. Zhao, Unveiling the origins of low lattice thermal conductivity in 122-phase Zintl compounds, Mater. Today Phys. 21 (2021) 100480. https://doi.org/10.1016/j.mtphys.2021.100480.
[11] X. Wang, W. Li, C. Wang, J. Li, X.Y. Zhang, B.Q. Zhou, Y. Chen, Y.Z. Pei, Single parabolic band transport in p-type $EuZn_2Sb_2$ thermoelectrics, J. Mater. Chem. A 5 (46) (2017) 24185–24192. https://doi.org/10.1039/c7ta08869h.
[12] X. Wang, J. Li, C. Wang, B.Q. Zhou, L.T. Zheng, B. Gao, Y. Chen, Y.Z. Pei, Orbital alignment for high performance thermoelectric $YbCd_2Sb_2$ alloys, Chem. Mater. 30 (15) (2018) 5339–5345. https://doi.org/10.1021/acs.chemmater.8b02155.
[13] K. Guo, Q.G. Cao, X.J. Feng, M.B. Tang, H.H. Chen, X. Guo, L. Chen, Y. Grin, J.-T. Zhao, Enhanced thermoelectric figure of merit of Zintl phase $YbCd_{2-x}Mn_xSb_2$ by chemical substitution, Eur. J. Inorg. Chem. 2011 (26) (2011) 4043–4048. https://doi.org/10.1002/ejic.201100282.
[14] J. Shuai, Z.H. Liu, H.S. Kim, Y.M. Wang, J. Mao, R. He, J.H. Sui, Z.F. Ren, Thermoelectric properties of Bi-based Zintl compounds $Ca_{1-x}Yb_xMg_2Bi_2$, J. Mater. Chem. A 4 (11) (2016) 4312–4320. https://doi.org/10.1039/c6ta00507a.
[15] A. Zevalkink, W.G. Zeier, E. Cheng, J. Snyder, J.P. Fleurial, S. Bux, Nonstoichiometry in the Zintl phase $Yb_{1-\delta}Zn_2Sb_2$ as a route to thermoelectric optimization, Chem. Mater. 26 (19) (2014) 5710–5717. https://doi.org/10.1021/cm502588r.
[16] K. Guo, J.W. Lin, Y. Li, Y.F. Zhu, X. Li, X.X. Yang, J.J. Xing, J. Yang, J. Luo, J. T. Zhao, Suppressing the dynamic precipitation and lowering the thermal conductivity for stable and high thermoelectric performance in $BaCu_2Te_2$ based materials, J. Mater. Chem. A 8 (10) (2020) 5323–5331. https://doi.org/10.1039/d0ta00245c.
[17] C.H. Yang, K. Guo, X.X. Yang, J.J. Xing, K. Wang, J. Luo, J.T. Zhao, Realizing High Thermoelectric Performance in $BaCu_{2-x}Ag_xTe_2$ through Enhanced Carrier Effective Mass and Point-Defect Scattering, ACS Appl. Energy Mater. 2 (1) (2019) 889–895. https://doi.org/10.1021/acsaem.8b01977.
[18] M.A. McGuire, A.F. May, D.J. Singh, M.H. Du, G.E. Jellison, Transport and optical properties of heavily hole-doped semiconductors $BaCu_2Se_2$ and $BaCu_2Te_2$, J. Solid State Chem. 184 (10) (2011) 2744–2750. https://doi.org/10.1016/j.jssc.2011.08.021.
[19] J. Li, L.D. Zhao, J.H. Sui, D. Berardan, W. Cai, N. Dragoe, $BaCu_2Se_2$ based compounds as promising thermoelectric materials, Dalton Trans. 44 (5) (2015) 2285–2293. https://doi.org/10.1039/c4dt03556a.
[20] K. Kurosaki, H. Uneda, H. Muta, S. Yamanaka, Thermoelectric properties of β-$BaCu_2S_2$, J. Alloys Compd. 388 (1) (2005) 122–125. https://doi.org/10.1016/j.jallcom.2004.06.086.
[21] W. Li, Z. Liu, G. Yang, First-principles study of electronic structure, elastic and anisotropic thermoelectric properties of $BaCu_2Se_2$, J. Alloys Compd. 695 (2017) 3682–3688. https://doi.org/10.1016/j.jallcom.2016.11.368.
[22] T.J. Zhu, Y.T. Liu, C.G. Fu, J.P. Heremans, J.G. Snyder, X.B. Zhao, Compromise and synergy in high-efficiency thermoelectric materials, Adv. Mater. 29 (30) (2017) 1605884. https://doi.org/10.1002/adma.201702816.
[23] Y. Pei, A.D. LaLonde, N.A. Heinz, X. Shi, S. Iwanaga, H. Wang, L. Chen, G. J. Snyder, Stabilizing the optimal carrier concentration for high thermoelectric efficiency, Adv. Mater. 23 (47) (2011) 5674–5678. https://doi.org/10.1002/adma.201103153.

[24] Z. Dashevsky, S. Shusterman, M.P. Dariel, I. Drabkin, Thermoelectric efficiency in graded indium-doped PbTe crystals, J. Appl. Phys. 92 (3) (2002) 1425–1430. https://doi.org/10.1063/1.1490152.
[25] V.L. Kuznetsov, L.A. Kuznetsova, A.E. Kaliazin, D.M. Rowe, High performance functionally graded and segmented Bi_2Te_3-based materials for thermoelectric power generation, J. Mater. Sci. 37 (14) (2002) 2893–2897. https://doi.org/10.1016/j.jallcom.2004.06.086.
[26] J. Rodriguez-Carvajal, Recent developments of the program FULLPROF, IUCr Commission on Powder Diffraction Newsletter 26 (2001) 12–19.
[27] S. Baroni, S.D. Gironcoli, A.D. Corso, P. Giannozzi, Phonons and related crystal properties from density-functional perturbation theory, Rev. Mod. Phys. 73 (2) (2001) 515–562. https://doi.org/10.1103/RevModPhys.73.515.
[28] G. Kresse, J. Furthmüller, Efficient iterative schemes for ab initio total-energy calculations using a plane-wave basis set, Phys. Rev. B 54 (16) (1996) 11169–11186. https://doi.org/10.1103/PhysRevB.54.11169.
[29] P.E. Blöchl, Projector augmented-wave method, Phys. Rev. B 50 (24) (1994) 17953–17979. https://doi.org/10.1103/physrevb.50.17953.
[30] J. Heyd, G.E. Scuseria, M. Ernzerhof, Hybrid functionals based on a screened Coulomb potential, J. Chem. Phys. 118 (18) (2003) 8207–8215. https://doi.org/10.1063/1.1668634.
[31] J.P. Perdew, K. Burke, M. Ernzerhof, Generalized gradient approximation made simple, Phys. Rev. Lett. 77 (18) (1996) 3865–3868. https://doi.org/10.1103/PhysRevLett.77.3865.
[32] C.E. Calderon, J.J. Plata, C. Toher, C. Oses, O. Levy, M. Fornari, A. Natan, M. J. Mehl, G. Hart, M.B. Mardelli, S. Curtarolo, The AFLOW standard for high-throughput materials science calculations, Comput. Mater. Sci. 108 (2015) 233–238. https://doi.org/10.1016/j.commatsci.2015.07.019.
[33] H.J. Monkhorst, J.D. Pack, Special points for Brillouin-zone integrations, Phys. Rev. B 13 (12) (1976) 5188–5192. https://doi.org/10.1103/PhysRevB.13.5188.
[34] H. Zhang, S.M. Li, D.D. Li, S.F. Jin, S.J. Shen, T.P. Ying, Z.P. Lin, K.K. Li, D.D. Yuan, H.Z. Zhao, Enhancement of the thermoelectric properties of $BaCu_2Se_2$ by potassium doping, Mater. Lett. 152 (2015) 117–120. https://doi.org/10.1016/j.matlet.2015.03.098.
[35] R. Viennois, D. Bérardan, C. Popescu, Crystal Structure, Lattice Dynamics, and Thermodynamic Properties of a Thermoelectric Orthorhombic $BaCu_2Se_2$ Compound, J. Phys. Chem. C 124 (25) (2020) 13627–13638. https://doi.org/10.1021/acs.jpcc.0c03964.
[36] D.F. Zou, H.R. Zheng, J.Y. Li, Comparative studies of the electronic structure and thermoelectric properties in orthorhombic and tetragonal $BaCu_2Se_2$ by first-principles calculations, RSC Adv. 6 (65) (2016) 60717–60722. https://doi.org/10.1039/c6ra10266b.
[37] Y. Xiao, L.D. Zhao, Charge and phonon transport in PbTe-based thermoelectric materials, npj Quant Mater 3 (1) (2018) 1–12. https://doi.org/10.1038/s41535-018-0127-y.
[38] T.J. Zhu, L.P. Hu, X.B. Zhao, J. He, New insights into intrinsic point defects in V_2VI_3 thermoelectric materials, Adv. Sci. 3 (7) (2016) 1600004–1600019. https://doi.org/10.1002/advs.201600004.
[39] I.T. Witting, T.C. Chasapis, F. Ricci, M. Peters, N.A. Heinz, G. Hautier, G.J. Snyder, The thermoelectric properties of bismuth telluride, Adv. Electron. Mater. 5 (6) (2019) 1800904. https://doi.org/10.1002/aelm.201800904.
[40] M. Tiadi, M. Battabyal, P.K. Jain, A. Chauhan, D.K. Satapathy, R. Gopalan, Enhancing the thermoelectric efficiency in p-type Mg_3Sb_2 via Mg site co-doping, Sustainable Energy Fuels 5 (14) (2021) 4104–4114. https://doi.org/10.1039/d1se00656h.
[41] B.C. Qin, D.Y. Wang, X.X. Liu, Y.X. Qin, J.F. Dong, J.F. Luo, J.W. Li, W. Liu, G. J. Tan, X.F. Tang, J.F. Li, J.Q. He, L.D. Zhao, Power generation and thermoelectric cooling enabled by momentum and energy multiband alignments, Science 373 (6554) (2021) 556–561. https://doi.org/10.1126/science.abi8668.
[42] S. Lany, A. Zunger, Assessment of correction methods for the band-gap problem and for finite-size effects in supercell defect calculations: Case studies for ZnO and GaAs, Phys. Rev. B 78 (23) (2008) 235104. https://doi.org/10.1103/PhysRevB.78.235104.
[43] S.Y. Wang, Y.X. Sun, J. Yang, B. Duan, L.H. Wu, W.Q. Zhang, J.H. Yang, High thermoelectric performance in $(Bi, Sb)_2Se_3$ via structural transition induced band convergence and chemical bond softening, Energy Environ. Sci. 9 (11) (2016) 3436–3447. https://doi.org/10.1039/c6ee02674e.
[44] W. Ren, Q. Song, H. Zhu, J. Mao, L. You, G.A. Gamage, J. Zhou, T. Zhou, J. Jiang, C. Wang, J. Luo, J. Wu, Z. Wang, G. Chen, Z. Ren, Intermediate-level doping strategy to simultaneously optimize power factor and phonon thermal conductivity for improving thermoelectric figure of merit, Mater. Today Phys. 15 (2020) 100250. https://doi.org/10.1016/j.mtphys.2020.100250.
[45] Y.D. Xu, W. Li, C. Wang, J. Li, Z.W. Chen, S.Q. Lin, Y. Chen, Y.Z. Pei, Performance optimization and single parabolic band behavior of thermoelectric MnTe, J. Mater. Chem. A 5 (36) (2017) 19143–19150. https://doi.org/10.1039/c7ta04842d.
[46] L. You, Y.F. Liu, X. Li, P.F. Nan, B.H. Ge, Y. Jiang, P.F. Luo, S.S. Pan, Y.Z. Pei, W. Q. Zhang, G.J. Snyder, J. Yang, J.Y. Zhang, J. Luo, Boosting the thermoelectric performance of PbSe through dynamic doping and hierarchical phonon scattering, Energy Environ. Sci. 11 (7) (2018) 1848–1858. https://doi.org/10.1039/c8ee00418h.
[47] L. You, J.Y. Zhang, S.S. Pan, Y. Jiang, K. Wang, J. Yang, Y.Z. Pei, Q. Zhu, M. T. Agne, G.J. Snyder, Z.F. Ren, W.Q. Zhang, J. Luo, Realization of higher thermoelectric performance by dynamic doping of copper in n-type PbTe, Energy Environ. Sci. 12 (10) (2019) 3089–3098. https://doi.org/10.1039/c9ee01137d.
[48] M. Ohta, P. Jood, M. Murata, C.-H. Lee, A. Yamamoto, H. Obara, An Integrated Approach to Thermoelectrics: Combining phonon dynamics, nanoengineering, novel Materials Development, module fabrication, and metrology, Adv. Energy Mater. 9 (23) (2019) 1801304. https://doi.org/10.1002/aenm.201801304.
[49] L. Bjerg, G.K. Madsen, B.B. Iversen, Enhanced Thermoelectric Properties in Zinc Antimonides, Chem. Mater. 23 (17) (2011) 3907–3914. https://doi.org/10.1021/cm201271d.
[50] J. Li, Y. Xie, C. Zhang, K. Ma, F. Liu, W. Ao, Y. Li, C. Zhang, Stacking fault-induced minimized lattice thermal conductivity in the high-performance GeTe-based thermoelectric materials upon Bi_2Te_3 alloying, ACS Appl. Mater. Interfaces 11 (22) (2019) 20064–20072. https://doi.org/10.1021/acsami.9b04984.